Materials Advances

ROYAL SOCIETY OF CHEMISTRY

PAPER

View Article Online
View Journal | View Issue

Cite this: *Mater. Adv.*, 2025, 6, 4211

In situ decorated Ni and Co in a CuBTC MOF for synergistic photocatalytic hydrogen generation†

Bhavya Jaksani,[ab] Janardhan Abburi,[a] Hafijul Islam,[ab] Spandana Gonuguntla,[c] Tinku Baidya[d] and Ujjwal Pal *[ab]

Received 14th December 2024,
Accepted 9th April 2025

DOI: 10.1039/d4ma01243g

rsc.li/materials-advances

In this study, a novel metal–organic framework (MOF), Co and Ni ion impregnated CuBTC, is synthesized and its photocatalytic hydrogen evolution reaction (HER) performance is investigated. The partial substitution of Cu^{2+} with Co^{2+} and Ni^{2+} ions in the catalyst is carried out and investigated to obtain critical insights into the underlying reaction mechanism. Morphological analysis revealed a well-defined octahedral structure for all photocatalysts. Among the synthesized materials, Co–Ni–CuBTC exhibited the highest HER rate of 23.9 mmol g^{-1} h^{-1}, which is 6.6 times higher than that of pristine CuBTC. The photocatalyst characterization and its improved performance were corroborated using various physicochemical analyses including XRD, FTIR, XPS, and UV-DRS, and thermal stability assessments *via* TGA analysis. The Co–Ni–CuBTC composite exhibited a significant surface area and a prolonged average photoexcited charge lifetime of 1.03 nanoseconds, enhancing its photocatalytic HER efficiency. The structural stability of the Co–Ni–CuBTC photocatalyst is confirmed through post reaction SEM and XRD investigations. The photocatalytic mechanism study emphasizes the synergistic role of Co^{2+} and Ni^{2+} in the CuBTC framework with desirable photo redox properties for a superior HER. This work offers a promising strategy for uniformly incorporating multiple metal sites into organic frameworks to synergistically enhance photocatalytic performance.

Introduction

Our society faces the dual challenges of an energy crisis and environmental pollution, and conventional energy sources are proving to be insufficient to meet growing demands while contributing heavily to ecological harm. In this context, there is a global consensus on the urgent need for clean and sustainable energy alternatives.[1,2] Hydrogen stands out as a clean, renewable energy source with versatile applications in fuel cells and energy storage systems.[3] Among the various production methods of green H_2, photocatalytic hydrogen production from water offers a green, promising pathway with its potential for reduced carbon emissions, high energy efficiency and utilization of abundant solar energy.[4,5] Researchers have developed numerous photocatalysts for H_2 production through photocatalytic water splitting, including metal oxides, sulfides, MOFs, layered double hydroxides (LDHs), and heterojunctions with various semiconductors.[6–10]

As emerging porous materials with stable structures, MOFs, a class of organic–inorganic hybrid crystalline solid materials, have been extensively used for a number of purposes, including catalysis, adsorption/separation, and more.[11] Basically, the unique structural characteristics of MOFs allow the frameworks to evenly integrate the catalytic active sites and light-harvesting centres.[12–16] The coordination of transition metals (Zn, Cu, Ni, Co and Fe) with 1,3,5-benzenetricarboxylic acid (BTC) produces metal–BTCs, which are among the MOFs that are widely utilized to create a variety of catalysts with distinct structures and purposes. Nevertheless, the majority of studies have concentrated on the use of metal–BTCs in gas adsorption and electrocatalysis, while their usage in photolysis as photocatalysts is rarely reported.[17,18] CuBTC (also known as HKUST-1 or $Cu_3(BTC)_2$, with BTC as the organic linker) has emerged as a promising photocatalytic material due to its high porosity, large surface area, tunable structure, and cost-effective large-scale synthesis. However, its application in hydrogen production *via* water photolysis is limited by the quick recombination of photogenerated charge carriers and structural degradation caused by the adsorption of water. As a result, the

[a] *Department of Energy & Environmental Engineering, CSIR-Indian Institute of Chemical Technology, Tarnaka, Hyderabad, Telangana-500007, India. E-mail: upal03@gmail.com, ujjwalpal@iict.res.in*
[b] *Academy of Scientific & Innovative Research (AcSIR), Ghaziabad Uttar Pradesh-201002, India*
[c] *Malla Reddy College of Engineering for Women, Maisammaguda, Dhulapally Kompally, Medchal Rd, M, Secunderabad, Telangana 500100, India*
[d] *Department of Chemistry, Koneru Lakshmaiah Education Foundation, Green Fields, Vaddeswaram, Guntur-522302, India*

† Electronic supplementary information (ESI) available. See DOI: https://doi.org/10.1039/d4ma01243g

photocatalytic activity of pure CuBTC remains relatively low.[19] To address these challenges, various strategies such as creating heterojunctions, incorporating additional metal dopants, and introducing defective ligands into CuBTC are used. These approaches aimed to enhance its specific surface area, electronic and spatial properties, light absorption capacity, bandgap, and charge carrier separation efficiency.[20–22]

Trimetallic MOFs with adjustable bandgaps are commonly synthesized by incorporating two or more metal ions into a single framework, resulting in multiple active sites. This integration enhances intramolecular self-assembly *via* coordination effects, thereby improving their overall efficiency.[23–27] In this study, we developed an innovative *in situ* method to synthesize Co–Ni–CuBTC by substituting Cu^{2+} with Ni^{2+} and Co^{2+} ions within the BTC framework through a solvothermal process at 120 °C. Co and Ni were selected for doping into CuBTC due to their abundance, economic viability, and ionic radii (Co^{2+}: 0.745 Å, Ni^{2+}: 0.69 Å, and Cu^{2+}: 0.73 Å), allowing partial exchange with minimal lattice distortion.[28,29] Co and Ni act as co-catalysts, facilitating more efficient charge separation and electron transfer, thereby minimizing electron–hole recombination. Their presence introduces additional active sites and modulates the electronic structure, optimizing the adsorption and activation of water molecules for enhanced hydrogen production. Furthermore, Co and Ni synergistically improved photoexcited charge transfer properties, conductivity and stability, ensuring prolonged photocatalytic activity. These combined effects significantly boost the HER performance compared to pristine CuBTC, demonstrating the effectiveness of our material design. Additionally, their synergy with the CuBTC porous structure and electronic properties establishes an efficient framework for photocatalysis. The resulted Co–Ni–CuBTC demonstrated effective photocatalytic hydrogen evolution (PHE) in aqueous methanol solutions and displayed a hydrogen production rate about six times higher than that of the pristine CuBTC under a simulated solar spectrum. Additionally, photocatalytic cycling stability tests confirmed the catalyst reusability and regenerative capacity. The findings highlighted several advantages of the Co–Ni–CuBTC catalyst, including enhanced light absorption, high lifetime, and sustained transient photocurrent, all contributing to significantly improved hydrogen production.

Experimental section

CuBTC was prepared using a reported method[18] and the synthesis of Ni–CuBTC and Co–CuBTC is detailed in the ESI.†

Preparation of Co–Ni–CuBTC

The synthesis of Co–Ni–CuBTC was performed by dissolving 1.27 g of $Cu(NO_3)_2{\cdot}3H_2O$, 0.24 g of $Co(NO_3)_2{\cdot}6H_2O$, and 0.290 g of $Ni(NO_3)_2{\cdot}6H_2O$ in 7.2 mL of deionized water and 0.840 g of 1,3,5-benzenetricarboxylic acid in 24 mL of ethanol. The two solutions were combined and stirred for 10 minutes, followed by the addition of 12 mL of isopropanol. The two solutions were subsequently placed into a Teflon-lined stainless-steel autoclave and subjected to heating in an oven at 120 °C for 12 hours. After cooling, the resulting material was collected *via* centrifugation. The obtained blue precipitate was washed three times with ethanol and dried at 80 °C overnight. By taking different molar ratios of Co^{2+} and Ni^{2+} by keeping Cu^{2+} constant, products were obtained and labelled as Co–Ni–CuBTC(1) and Co–Ni–CuBTC(2) (Scheme 1) and are shown in Table 1.

Results and discussion

Powder XRD analysis verified the successful synthesis and crystal phase of CuBTC, as well as Ni–CuBTC, Co–CuBTC, and Co–Ni–CuBTC. The diffraction patterns for all samples displayed identical peak positions, with characteristic peaks observed at 2θ values of 6.7°, 9.7°, 11.7°, 13.5°, and 19.1° corresponding to the (200), (220), (222), (400), and (440) planes

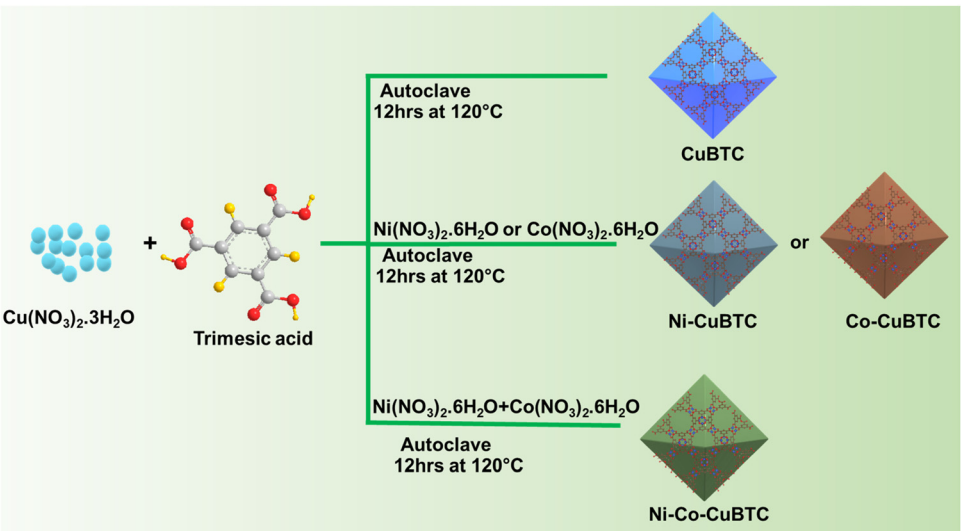

Scheme 1 Synthesis process diagram for CuBTC, Ni–CuBTC, Co–CuBTC, and Co–Ni–CuBTC.

Table 1 Contents of metal salts used in the synthesis of MOFs and metal concentrations obtained from ICP-MS

S. no.	Photocatalyst	Theoretical (millimoles)			ICP-MS (ppb)		
		Co^{2+}	Ni^{2+}	Cu^{2+}	Co^{2+}	Ni^{2+}	Cu^{2+}
1.	CuBTC	0	0	7.3	—	—	24 801.62
2.	Co–CuBTC	2	0	5.3	1647.11	—	12 833.76
3.	Ni–CuBTC	0	2	5.3	—	1636.96	17 460.43
4.	Co–Ni–CuBTC	1	1	5.3	1809.50	2291.68	19 341.75
5.	Co–Ni–CuBTC(1)	1.5	0.5	5.3	—	—	—
6.	Co–Ni–CuBTC(2)	0.5	1.5	5.3	—	—	—

of CuBTC, as illustrated in Fig. 1(a). These diffraction results align with previously reported data, supporting the successful formation of CuBTC and the patterns closely matched the reference JCPDS card no. 00-064-0936.[30,31] Ni–CuBTC, Co–CuBTC, and Co–Ni–CuBTC exhibited identical peaks at the same 2θ positions as CuBTC, confirming the preservation of the MOF structure and indicating that Ni and Co incorporation did not introduce phase impurities or structural changes in CuBTC.[32]

The FTIR spectra of the fabricated photocatalysts display distinctive peaks and confirm structural details (Fig. 1(b)). Peaks at 488 cm^{-1} and 721 cm^{-1} correspond to the bending and stretching vibrations of Cu-O, verifying the coordination between BTC ligands and Cu^{2+} ions.[33] A strong absorption peak at 1642 cm^{-1} is attributed to the C═O bonds within the BTC linkers of the CuBTC structure, indicating the presence of carboxyl groups essential for metal–ligand coordination. Additionally, intense peaks at 1365 cm^{-1} and 1444 cm^{-1} are associated with the asymmetric and symmetric stretching modes of C–O and C═C bonds, respectively.[34] The bending vibration peak of C–H appears at 938 cm^{-1}, while a broad band at 3346 cm^{-1} suggests the presence of surface-adsorbed water and hydroxyl groups within the CuBTC framework.[35] All synthesized photocatalysts exhibit these same characteristic peaks, confirming the presence of the CuBTC structure in all samples.

X-ray photoelectron spectroscopy (XPS) was employed to analyse the surface composition and chemical states of the photocatalysts. The survey spectra in Fig. 2(a) confirmed the existence of C 1s, O 1s, Cu 2p, Co 2p, and Ni 2p peaks in Co–Ni–CuBTC. The C 1s spectrum shown in Fig. 2(b) of Co–Ni–CuBTC reveals three distinct peaks at 284.8 eV (C═C), 286.1 eV (C–O), and 288.6 eV (C═O).[36,37] The O 1s spectrum shown in Fig. 2(c) exhibits main peaks around 531.7 eV and 532.8 eV, corresponding to lattice oxygen and C–O functional groups.[38,39] The Cu 2p spectrum shown in Fig. 2(d) reveals two peaks at 954.04 eV and 934.02 eV for Cu $2p_{1/2}$ and $2p_{3/2}$ with satellite peaks at 940 eV and 943.9 eV confirming the Cu^{2+} presence.[20] The binding energy peaks detected at 781.8 eV and 797.1 eV for Co $2p_{3/2}$ and Co $2p_{1/2}$, with satellite peaks at 786.2 eV and 802.3 eV, indicate Co^{2+} coordination through chemical interactions, Fig. 2(e).[38] In the Ni 2p region (Fig. 2(f)), the Ni $2p_{3/2}$ and Ni $2p_{1/2}$ peaks appeared at 856.2 eV and 874.1 eV, confirming the Ni^{2+} oxidation state, with satellite peaks at 861.4 eV and 880.5 eV.[40,41] To investigate differential charging, we compared the XPS profiles of C 1s, O 1s, and Cu 2p for CuBTC (Fig. S3(a)–(c), ESI†) and Co–Ni–CuBTC. A noticeable shift in binding energy (B.E.) values and variations in peak intensities of C 1s and O 1s were observed in CuBTC compared to Co–Ni–CuBTC. In the Cu 2p spectrum of CuBTC, the Cu $2p_{1/2}$ and Cu $2p_{3/2}$ peaks appear at 954.28 eV and 934.24 eV, respectively, indicating a negative shift in Co–Ni–CuBTC attributed to the decreased electron density around Cu centers due to the incorporation of Co and Ni into CuBTC. Collectively, these XPS results confirm the formation of the tri-metallic Co–Ni-CuMOF, with Co, Ni, and Cu ions bound to tricarboxylate linkers in the CuBTC structure.

FESEM analysis reveals the morphological features of CuBTC and Co–Ni–CuBTC. The particles of CuBTC and Co–Ni–CuBTC exhibit an octahedral geometry with smooth surfaces, as shown in Fig. 3(a)–(d). The SEM images of Co–CuBTC and Ni–CuBTC are provided in Fig. S1, ESI.† However, some

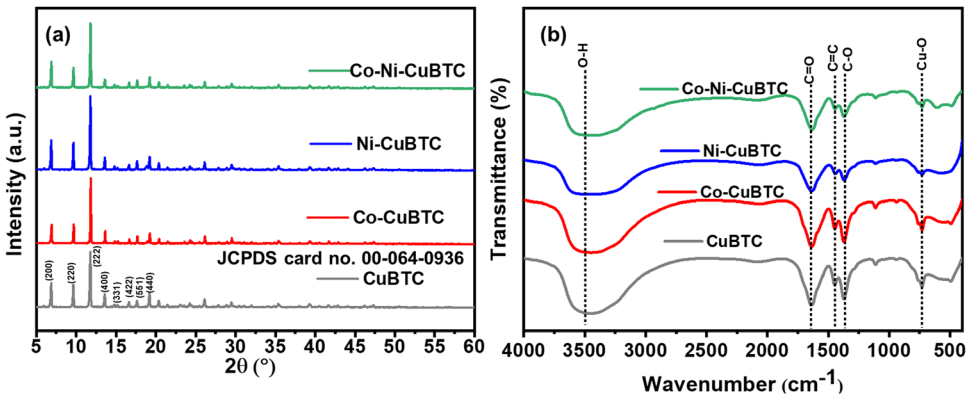

Fig. 1 (a) PXRD patterns, and (b) FTIR spectra of CuBTC, Ni–CuBTC, Co–CuBTC and Co–Ni–CuBTC.

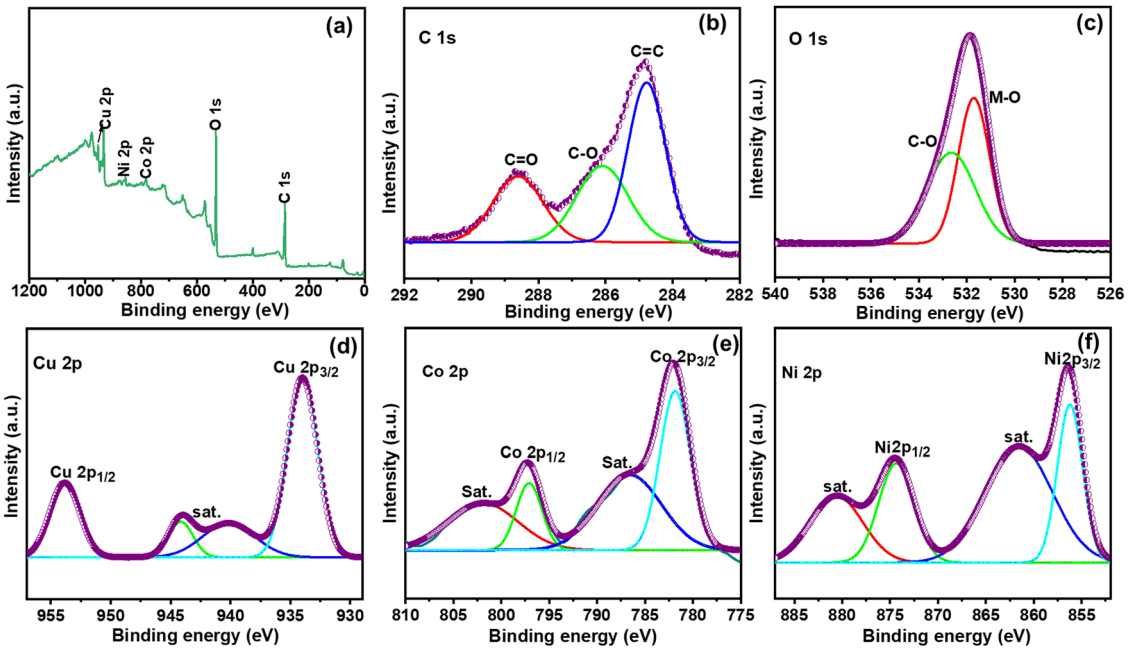

Fig. 2 XPS spectra of Co–Ni–CuBTC: (a) survey spectra, (b) C 1s, (c) O 1s, (d) Cu 2p, (e) Co 2p and (f) Ni 2p.

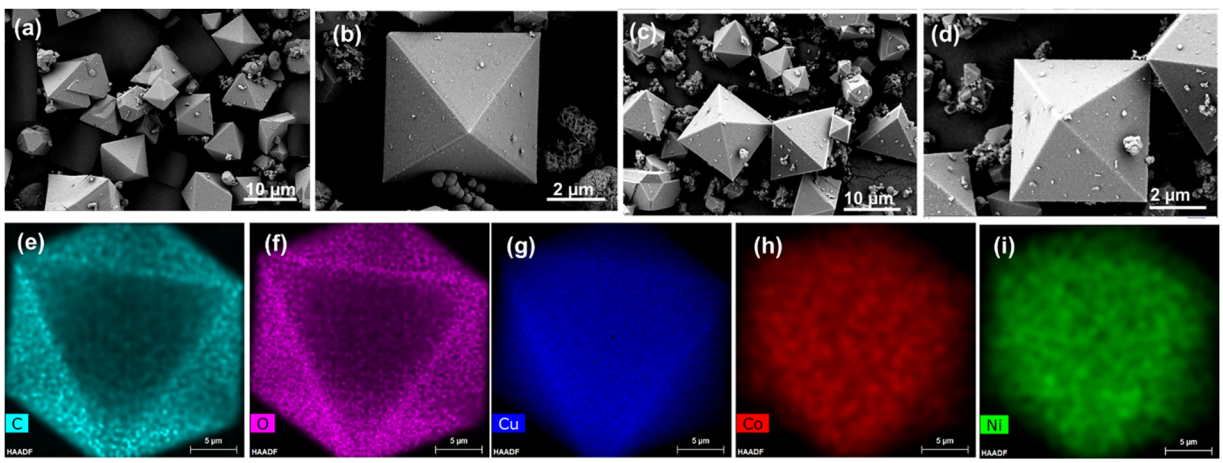

Fig. 3 FESEM images of (a) and (b) CuBTC, (c) and (d) Co–Ni–CuBTC. HAADF-STEM images of Co–Ni–CuBTC (e) C, (f) O, (g) Cu, (h) Co, and (i) Ni.

variations in the particle size and shape were observed indicating moderate non-uniformity. Notably, no substantial morphological differences were detected in the CuBTC structure before and after Co and Ni inclusion.[42] EDS analysis confirmed the presence of Co and Ni on the catalyst surface (Fig. S2, ESI†) and the absence of significant changes in the morphology suggests the successful incorporation of Co and Ni into the CuBTC surface. High-angle annular dark-field scanning transmission electron microscopy (HAADF-STEM) confirmed the presence of Co and Ni metal atoms in Co–Ni–CuBTC (Fig. 3(e)–(i)). The octahedral shape indicated that the inclusion of Co and Ni did not alter the morphology of CuBTC. Additionally, HAADF-STEM elemental mapping demonstrated a uniform distribution of Co, Ni, Cu, C, and O elements throughout the structure, with no evidence of aggregation. The concentrations of Cu^{2+}, Co^{2+}, and Ni^{2+} in the synthesized MOFs were determined using ICP-MS, as presented in Table 1.

UV-DRS spectra of CuBTC samples were recorded to assess their light-harvesting potential. The spectra revealed a distinct absorption between 200 and 350 nm, attributed to ligand-to-metal charge transfer (LMCT) from oxygen to Cu^{2+} ions (Fig. 4(a)).[21,43,44] When Co and Ni were incorporated into the CuBTC framework, the LMCT band of the Co–Ni–CuBTC composite exhibited a red-shift and gradually increased light absorption, relative to CuBTC. These enhanced characteristics suggest that the composite structure is well-suited for visible-light photocatalysis. The band gap energies of the photocatalysts were determined using the Kubelka–Munk equation [$\alpha h\nu =$

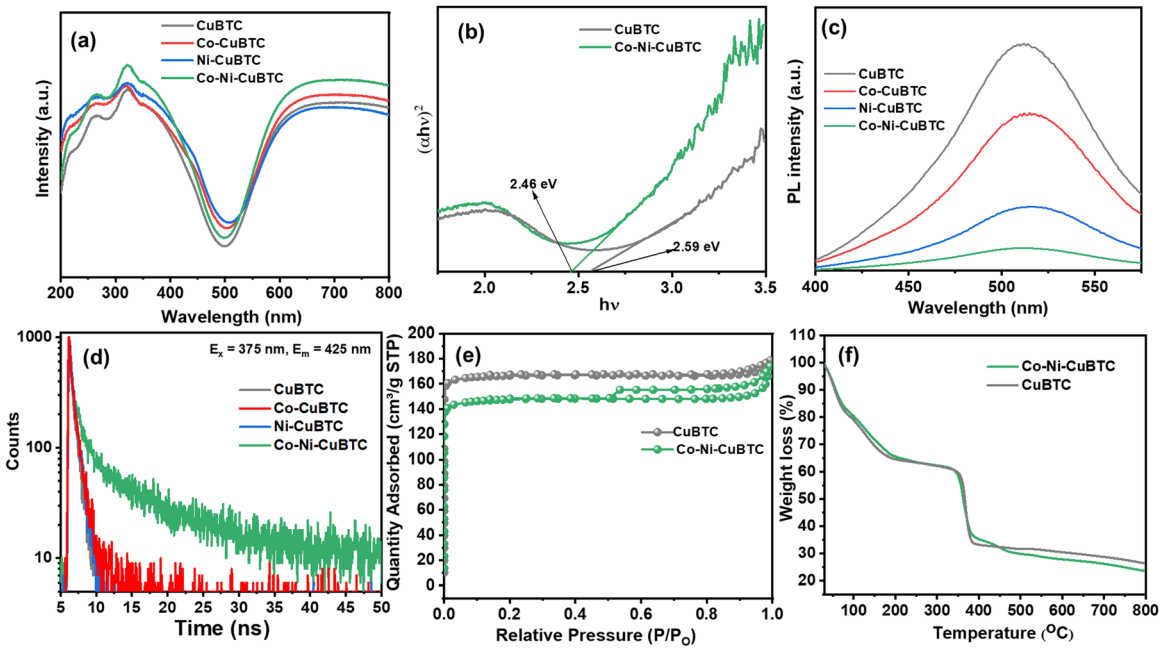

Fig. 4 (a) UV-DRS plots, (b) Tauc plots, (c) PL spectra, (d) TCSPC analysis, (e) N_2 adsorption–desorption isotherm, and (f) TGA plots of the prepared composites.

Table 2 Surface area and pore size parameters of CuBTC and Co–Ni–CuBTC

S. no	Photocatalyst	BET surface area ($m^2\ g^{-1}$)	Langmuir surface area ($m^2\ g^{-1}$)	Pore size (nm)	Pore volume ($cm^3\ g^{-1}$)
1	CuBTC	695.194	725.408	9.845	0.023
2	Co–Ni–CuBTC	611.1253	645.1855	13.091	0.046

$A(h\nu - E_g)^2$]. CuBTC and Co–Ni–CuBTC show band-gap energies of 2.59 eV and 2.46 eV, respectively (Fig. 4(b)) consistent with reported literature.[21,45] The photoluminescence (PL) spectra show fluorescence from the recombination of photogenerated electrons and holes (Fig. 4(c)). Upon excitation at 300 nm, the emission peak occurs at approximately 525 nm.[46] The Co–Ni–CuBTC composite shows a significant reduction in emission intensity, indicating rapid charge transfer kinetics and a lower recombination rate of electron–hole pairs, which facilitate an enhanced rate for PHE. The charge carrier dynamics were investigated using time-resolved photoluminescence spectroscopy (TRPL). This analysis revealed lifetimes of CuBTC (0.51 ns), Ni–CuBTC (0.57 ns), Co–CuBTC (0.63 ns), and Ni–Co–CuBTC (1.03 ns) as shown in Fig. 4(d). The extended lifetime in Ni–Co–CuBTC is due to modified electron–hole recombination and quenching effects, enhanced charge transfer, light harvesting, and PHE.

Brunauer–Emmett–Teller (BET) analysis, along with BJH pore size distribution curves were utilized to determine the specific surface area and pore volume of CuBTC and Co–Ni–CuBTC through N_2 adsorption–desorption isotherms. The CuBTC sample exhibited a high surface area of 695 $m^2\ g^{-1}$, with a pore size of 9.84 nm and a pore volume of 0.023 $cm^3\ g^{-1}$. After the incorporation of Co^{2+} and Ni^{2+} ions, the surface area of Co–Ni–CuBTC was adjusted to 611.12 $m^2\ g^{-1}$, with an increased pore size of 13.09 nm and a pore volume of 0.046 $cm^3\ g^{-1}$. The decrease in the surface area and an increase in the pore size and pore volume in Co–Ni–CuBTC, relative to CuBTC, are ascribed to the partial exchanging of Cu^{2+} ions with Co^{2+} and Ni^{2+}, which alters the pore structure.[25] Both samples exhibited a microporous structure with a type I adsorption–desorption isotherm (Fig. 4(e) and Fig. S4(a), (b), ESI†), and the surface area data are provided in Table 2.

The thermogravimetric analysis (TGA) related to the as-synthesized CuBTC and Co–Ni–CuBTC samples is illustrated in Fig. 4(f). A slight weight reduction of 15% was observed for CuBTC within the temperature range of 40 to 70 °C, which can be ascribed to the elimination of H_2O molecules. A subsequent reduction in mass of 20% was noted between 75 and 180 °C, indicative of the escape of solvent molecules from the CuBTC framework. When temperatures exceed 380 °C, a notable weight reduction of around 35% was recorded, attributed to the breakdown of the BTC framework, resulting in the formation of H_2O, CO_2, and Cu_2O. The TGA profile of Co–Ni–CuBTC closely resembles that of CuBTC, suggesting that both MOFs demonstrate thermal behaviour up to 380 °C.[29,47,48]

Photocatalytic hydrogen evolution

Under light irradiation, the PHE performance of each synthesized photocatalyst was evaluated by suspending 10 mg of the

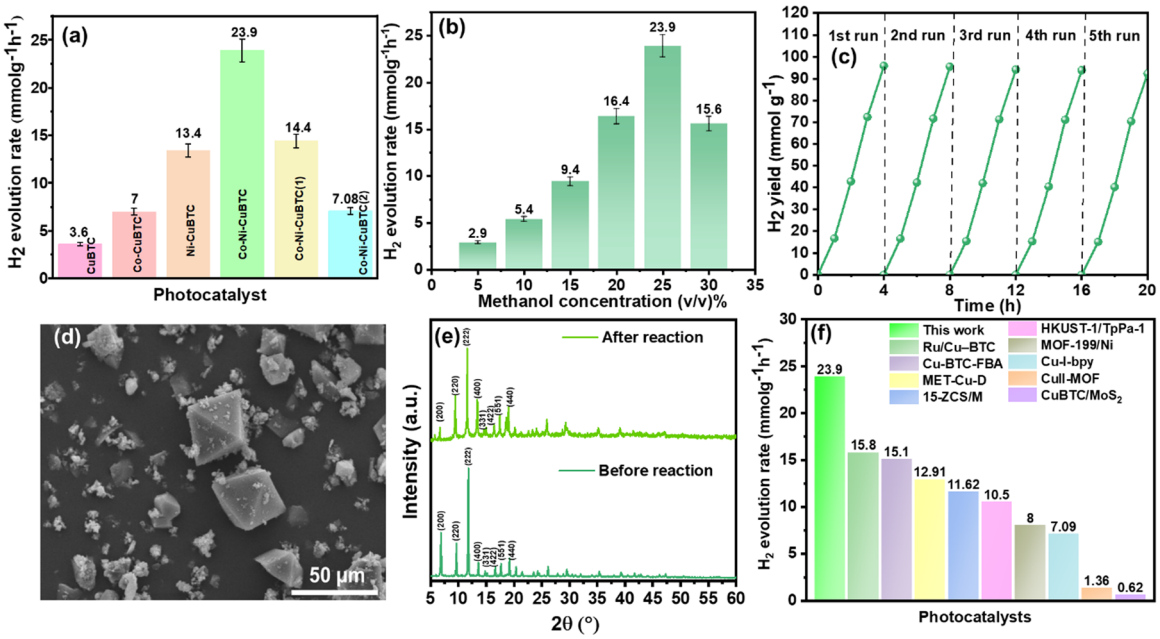

Fig. 5 (a) Histogram showing PHE rates of synthesised photocatalysts, (b) PHE rates of Co–Ni–CuBTC at various methanol concentrations, (c) stability test of the optimised catalyst (Co–Ni–CuBTC), (d) SEM images, (e) PXRD pattern of Co–Ni–CuBTC before and after the photocatalytic reaction, and (f) Comparison of PHE rates between Co–Ni–CuBTC and CuBTC-based photocatalysts.

catalyst in a mixed aqueous solution comprising 25 mL of deionized water and 25 mL of methanol (1 : 1) which served as sacrificial electron donor. During illumination, photogenerated excitons are created and migrated to specific energetic band positions, thereby triggering critical redox reactions. The PHE results of synthesised MOFs depicted in Fig. 5(a), Table S1 (ESI†) demonstrate HER rates that follow a distinct progression: Co–Ni–CuBTC > Co–Ni–CuBTC (1) > Ni–CuBTC > Co–Ni–CuBTC (2) > Co–CuBTC > CuBTC. Notably, Co–Ni–CuBTC exhibited the most exceptional hydrogen generation rate, reaching 23.9 mmol g^{-1} h^{-1}. The accompanying comparative data suggest that strategic metal exchange of Co and Ni in CuBTC is crucial for optimizing hydrogen production with the caution that excessive metal incorporation can potentially diminish photocatalytic efficiency. The hydrogen production of the optimized catalyst (Co–Ni–CuBTC) was evaluated at various methanol concentrations. As shown in Fig. 5(b), hydrogen evolution increased significantly with increasing methanol concentrations peaking at 50% (v/v), and above this concentration PHE declined drastically. This shows that greater methanol concentrations increase photocatalyst methanol adsorption and for methanol decomposition, additional reactive species ($^{\bullet}$OH) are needed. Due to consistent light intensity, irradiation period, and catalyst quantity, $^{\bullet}$OH generation does not increase. Thus, methanol breakdown efficiency drops reducing hydrogen generation at methanol concentrations above 50% (v/v).[49] The strategic incorporation of Co^{2+} and Ni^{2+} significantly amplifies CuBTC visible-light photocatalytic performance. Apparent quantum efficiency (AQE) data reveal that Co–Ni–CuBTC outperforms other composites, demonstrating the highest AQE of 57.3%. The photocatalytic stability test conducted over five cycles showed impressive efficiency, with only a 4% decline (Fig. 5(c)). Comprehensive post-reaction analyses including SEM, XRD and XPS were conducted. The SEM image of the catalyst after the reaction (Fig. 5(d)) confirms the negligible morphological alterations revealing catalyst structural integrity. The XRD pattern of the catalyst before and after the photocatalytic reaction (Fig. 5(e)) displays nearly identical peaks. However, the post-reaction catalyst exhibits slightly reduced peak intensity and broader profiles, suggesting a possible decrease in crystallinity. The appearance of small peaks after the reaction may indicate MOF surface corrosion and interference from decomposed sacrificial electron donors during photo-irradiation. XPS analysis of Co–Ni–CuBTC (Fig. S5(a)–(e), ESI†) after photocatalysis confirmed that Co, Ni, and Cu maintained their +2 oxidation states throughout the reaction. These demonstrates the exceptional chemical stability of the Co–Ni–CuBTC framework during photocatalytic processes. Among CuMOF-based photocatalysts, Co–Ni–CuBTC exhibited remarkable photocatalytic performance, as illustrated in Fig. 5(f) and Table S2 (ESI†).

Photoelectrochemical properties of photocatalysts

To assess the charge transfer capabilities of photocatalysts, several photoelectrochemical analysis techniques were used, including transient photocurrent measurements, electrochemical impedance spectroscopy (EIS), and Mott–Schottky analysis. When comparing the photocurrent of synthesised MOFs, Co–Ni–CuBTC demonstrated the highest photocurrent density which aligns with the PHE performance suggesting that the charge separation was improved and the charge recombination was decreased at the CuBTC-metal ion interface after doping metal ions (Co, Ni) into CuBTC, as shown in Fig. 6(a).[50] Photocurrent measurement of Co–Ni–CuBTC extended to 30 minutes,

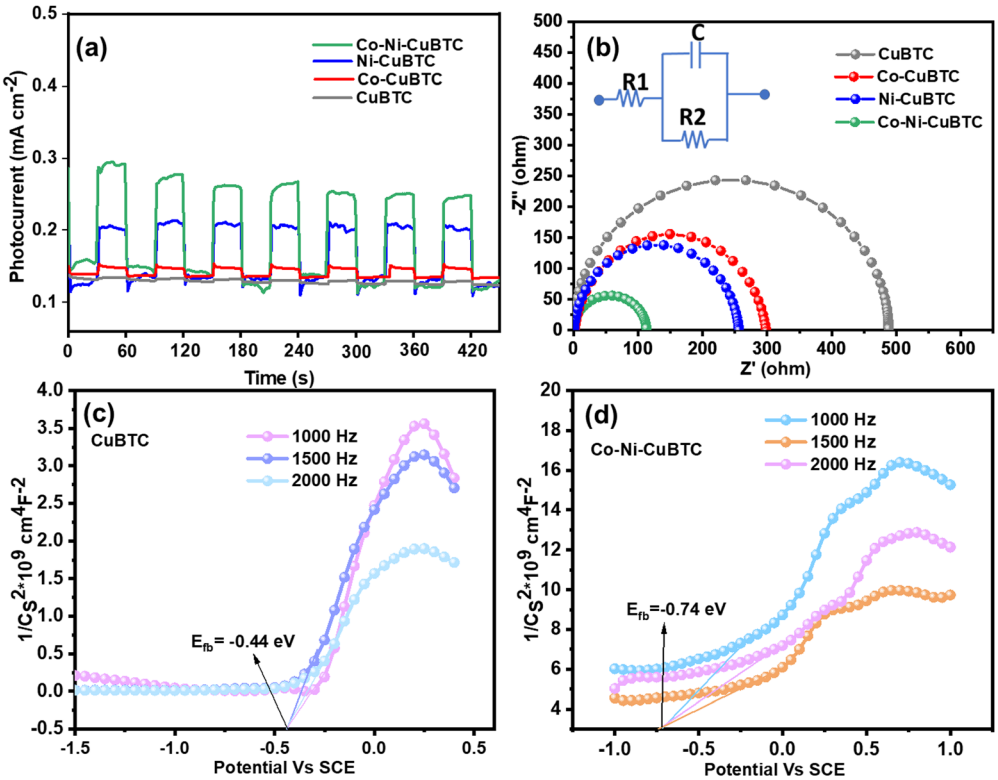

Fig. 6 (a) Transient photocurrent plots, (b) EIS plots of synthesised photocatalysts. The inset shows the equivalent circuit, Mott–Schottky plots of (c) CuBTC and (d) Co–Ni–CuBTC.

and it exhibited a sustained photocurrent response, demonstrating excellent charge separation efficiency and long-term stability under continuous illumination (Fig. S6, ESI†). Co–Ni–CuBTC displayed the smallest EIS curves, which means that the interfacial charge transfer resistance was lowered when Ni^{2+} and Co^{2+} were introduced to the CuBTC framework (Fig. 6(b)).[51] Mott–Schottky analysis was used to evaluate the conduction band positions of semiconductor materials. As shown in Fig. (6(c) and (d)), both CuBTC and Co–Ni–CuBTC demonstrate typical n-type semiconductor behaviour. The flat band potentials of CuBTC and Co–Ni–CuBTC were positioned at −0.44 eV for CuBTC and −0.74 eV for Co–Ni–CuBTC, respectively, relative to the SCE.[52] Typically, in n-type semiconductors, the conduction band energy level (E_{CB}) is generally located about 0.1 to 0.2 eV more negative to the flat band potential (E_{FB}). Based on theoretical calculations, the E_{CB} values for CuBTC and Co–Ni–CuBTC are −0.64 eV and −0.94 eV *versus* SCE, respectively. Using the equation $E_{NHE} = E_{SCE} + 0.241$,[53] the E_{CB} values can be roughly estimated as −0.39 eV and −0.69 eV, respectively, relative to the NHE.

Photocatalytic mechanism

According to the findings derived from the Tauc plots and Mott–Schottky graphs, the band gap (E_g) values for CuBTC and Co–Ni–CuBTC were determined to be 2.59 eV and 2.46 eV, respectively. Furthermore, the E_{CB} values for CuBTC and Co–Ni–CuBTC were found to be −0.39 V and −0.69 V, respectively.

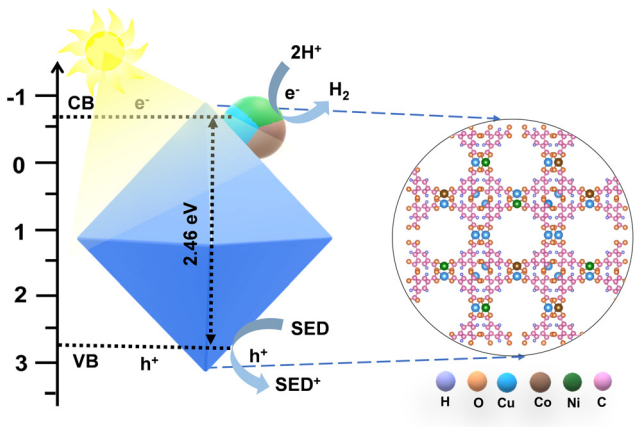

Fig. 7 Proposed mechanism for PHE through Co–Ni–CuBTC.

By using these, the valence band energy level (E_{VB}) can be calculated using formula $E_{VB} = E_{CB} + E_g$. The E_{VB} values of CuBTC and Co–Ni–CuBTC were obtained as 2.19 eV and 1.77 eV. A proposed mechanism for the PHE of Co–Ni–CuBTC is displayed in Fig. 7. Under light illumination, the BTC in the Co–Ni–CuBTC lattice absorbs visible light, resulting in the transition of photogenerated electrons from its excited state to the CB of the metal clusters through the LMCT mechanism creating holes at the VB of the organic linker (eqn (1)).[54] The water molecules adhering to the photocatalyst are reduced by

the electrons in the CB resulting in the production of H_2 (eqn (2) and (3)) Concurrently, the holes in the VB are captured by methanol, which undergoes oxidation generating H^+ ions (eqn (4)–(6)). These ions are subsequently reduced by excited electrons to yield hydrogen. The sequential procedure of photocatalytic hydrogen evolution *via* Co–Ni–CuBTC utilizing methanol as a sacrificial electron donor can be defined as[55,56]

$$\text{Co}-\text{Ni}-\text{CuBTC} \xrightarrow{h\nu} h^+ + e^- \quad (1)$$

$$H_2O + h^+ \rightarrow {}^{\bullet}OH + H^+ \quad (2)$$

$$2H^+ + 2e^- \rightarrow H_2 \quad (3)$$

$$CH_3OH + 2h^+ \rightarrow HCHO + 2H^+ \quad (4)$$

$$HCHO + H_2O + 2h^+ \rightarrow HCHO + 2H^+ \quad (5)$$

$$HCOOH + 2h^+ \rightarrow CO_2 + 2H^+ \quad (6)$$

$$\text{Overall reaction: } CH_3OH + H_2O(\text{Co}-\text{Ni}-\text{CuBTC}) \xrightarrow{h\nu} CO_2 + 3H_2 \quad (7)$$

Our study presents a novel Co–Ni–CuBTC catalyst, where the systematic incorporation of Co and Ni significantly enhances photocatalytic performance compared to conventional CuBTC by reducing the band gap, thereby enhancing visible light absorption. Co–Ni–CuBTC is identified as an effective photocatalyst due to its reduced fluorescence emission, indicating a decrease in charge carrier recombination and an extended carrier lifetime relative to CuBTC and other MOFs reported in the literature, as confirmed by TCSPC analysis and PL studies. The increased photocurrent and a reduced EIS radius observed in PEC studies suggest that Co and Ni facilitate charge carrier separation and lower charge transfer resistance relative to CuBTC. This synergistic interaction provides a greater number of active sites leading to higher hydrogen evolution rates and enhanced stability under prolonged photocatalytic conditions underscoring the unique advantages of our material design.

Conclusion

In conclusion, a novel Co–Ni–CuBTC MOF-based photocatalyst has been synthesized, featuring uniformly dispersed metal ions integrated *in situ* into the MOF, and is utilized for PHE. The optimized metal concentration in CuBTC resulted in a superior result in the HER with a rate of 23.9 mmol g^{-1} h^{-1} under visible light irradiation accompanied by an AQE of 57.3% at 420 nm. The synergistic interaction of uniformly distributed Co and Ni ions not only optimizes the utilization of visible light but also reduces the electron transfer distance thereby enhancing the efficiency of charge separation and transfer. This study introduces a straightforward method for uniformly arranging multimetal sites within a photocatalyst to enhance photocatalytic performance.

Data availability

The data supporting this article have been included as part of the ESI.†

Conflicts of interest

There are no conflicts to declare.

Acknowledgements

This work is supported by the HPCL (project no: CLP-0138/HPCL) and DST INSPIRE fellowship (IF 220088). B. J. thank DST and AcSIR for their PhD enrolment. We thank Dr D. Srinivasa Reddy, Director, Dr A. Gangagni Rao, HOD, DEEE in CSIR-IICT for all research facilities. CSIR-IICT Communication no: IICT/Pubs./2024/436.

References

1 S. D. Kshirsagar, S. P. Shelake, B. Biswas, K. Ramesh, R. Gaur, B. M. Abraham, A. V. S. Sainath and U. Pal, *Small*, 2024, **20**, 2407318.
2 A. Jamma, S. Pal, U. Pal and S. Ghosh, *Energy Fuels*, 2024, **38**, 23299–23319.
3 S. P. Shelake, D. N. Sutar, B. M. Abraham, T. Banerjee, A. V. S. Sainath and U. Pal, *Adv. Funct. Mater.*, 2024, **34**, 2403795.
4 S. Gonuguntla, B. Jaksani, A. Jamma, C. S. Vennapoosa, D. Chatterjee and U. Pal, *WIREs Energy Environ.*, 2024, **13**, e530.
5 A. Jamma, B. Jaksani, C. S. Vennapoosa, S. Gonuguntla, S. Sk, M. Ahmadipour, M. Abraham B, I. Mondal and U. Pal, *Mater. Adv.*, 2024, **5**, 2785–2796.
6 E. N. Musa, A. K. Yadav, K. T. Smith, M. S. Jung, W. F. Stickle, P. Eschbach, X. Ji and K. C. Stylianou, *Angew. Chem., Int. Ed.*, 2024, **63**, e202405681.
7 S. Gonuguntla, C. S. Vennapoosa, B. M. Abraham, A. V. S. Sainath and U. Pal, *ACS Appl. Nano Mater.*, 2024, **7**, 18146–18156.
8 S. D. Kshirsagar, S. P. Shelake, H. Islam, S. Bhattacharyya, M. Ahmadipour, A. V. Sesha Sainath and U. Pal, *Int. J. Hydrogen Energy*, 2024, DOI: 10.1016/j.ijhydene.2024.08.516.
9 C. S. Vennapoosa, S. P. Shelake, B. Jaksani, A. Jamma, B. Moses Abraham, A. V. Sesha Sainath, M. Ahmadipour and U. Pal, *Mater. Adv.*, 2024, **5**, 4159–4171.
10 S. D. Kshirsagar, S. P. Shelake, B. Biswas, A. Singh, S. Pakhira, A. V. Sesha Sainath and U. Pal, *Catal. Today*, 2025, **445**, 115056.
11 S. Sk, H. Islam, B. M. Abraham, I. Mondal and U. Pal, *Small Methods*, 2024, 2401689.
12 L. Liu, S. Du, X. Guo, Y. Xiao, Z. Yin, N. Yang, Y. Bao, X. Zhu, S. Jin, Z. Feng and F. Zhang, *J. Am. Chem. Soc.*, 2022, **144**, 2747–2754.
13 K. Zhang, H. Hu, L. Shi, B. Jia, H. Huang, X. Han, X. Sun and T. Ma, *Small Sci.*, 2021, **1**, 2100060.

14 T. K. Saothayanun, Y. Inchongkol, N. Weeranoppanant, M. Kondo, M. Ogawa and S. Bureekaew, *J. Mater. Chem. A*, 2024, **12**, 26743–26748.
15 E. M. El-Fawal, A. M. El Naggar and A. S. Morshedy, *Energy Convers. Manage.*, 2024, **320**, 118975.
16 C. I. Ezugwu, S. Ghosh, S. Bera, M. Faraldos, M. E. Mosquera and R. Rosal, *Sep. Purif. Technol.*, 2023, **308**, 122868.
17 M. Liao, H. Qin, W. Guo, P. Gao, J. Liu and H. Xiao, *Int. J. Hydrogen Energy*, 2022, **47**, 35136–35148.
18 N. Nurlan, M. Nurmyrza, S. Han and W. Lee, *Chem. Eng. J.*, 2024, **489**, 151276.
19 Y. Li, J. Miao, X. Sun, J. Xiao, Y. Li, H. Wang, Q. Xia and Z. Li, *Chem. Eng. J.*, 2016, **298**, 191–197.
20 Y. Ru, Y. Chen, X. Yu, Q. Zhang, Y. Yin and G. Tian, *Chem. Eng. J.*, 2023, **475**, 146158.
21 J. Xia, X. Liu, H. Zhou, L. Pu, J. Zhang, X. Li, F. Li, L. Long, S. Li and Y. He, *J. Catal. Sci. Technol.*, 2021, **11**, 7905–7913.
22 L. Zhang, C. Guo, T. Chen, Y. Guo, A. Hassan, Y. Kou, C. Guo and J. Wang, *Appl. Catal., B*, 2022, **303**, 120888.
23 M. Hu, J. Liu, S. Song, W. Wang, J. Yao, Y. Gong, C. Li, H. Li, Y. Li and X. Yuan, *ACS Catal.*, 2022, **12**, 3238–3248.
24 S. Zhang, L. Lu, J. Jiang, N. Liu, B. Zhao, M. Xu, P. Cheng and W. Shi, *Adv. Mater.*, 2024, 2403464.
25 A. Melillo, M. Cabrero-Antonino, S. Navalón, M. Álvaro, B. Ferrer and H. Garcia, *Appl. Catal., B*, 2020, **278**, 119345.
26 C. Li, H. Yu, S. Guo, J. Jia, Y. Chang, M. Jia and J. Wang, *New J. Chem.*, 2024, **48**, 3364–3369.
27 H. Han, H. Cui, J. Wang, K. Ge and Y. Yang, *ChemistrySelect*, 2024, **9**, e202403927.
28 W. Cheng, Z.-P. Wu, D. Luan, S.-Q. Zang and X. W. Lou, *Angew. Chem.*, 2021, **60**, 26397–26402.
29 A. M. P. Peedikakkal and I. H. Aljundi, *ACS Omega*, 2020, **5**, 28493–28499.
30 Y. Chen, Y. Ding, W. Han, W. Li, X. Yu and G. Tian, *J. Mater. Chem. A*, 2023, **11**, 8342–8351.
31 S. Dong, Z. Li, Y. Fu, G. Zhang, D. Zhang, M. Tong and T. Huang, *J. Electroanal. Chem.*, 2020, **858**, 113785.
32 F. Li, M. Ao, G. H. Pham, J. Sunarso, Y. Chen, J. Liu, K. Wang and S. Liu, *Small*, 2020, **16**, 1906276.
33 R. Kaur, A. Kaur, A. Umar, W. A. Anderson and S. K. Kansal, *Mater. Res. Bull.*, 2019, **109**, 124–133.
34 X. Xue, Y. Weng, S. Yang, S. Meng, Z. Zhang, G. Yi and Y. Zhang, *Environ. Sci. Pollut. Res.*, 2021, **28**, 15883–15889.
35 A. S. Morshedy, H. M. Abd El Salam, A. M. El Naggar and T. Zaki, *Energy Fuels*, 2020, **34**, 11660–11669.
36 M. F. Sanad, A. R. Puente Santiago, S. A. Tolba, M. A. Ahsan, O. Fernandez-Delgado, M. Shawky Adly, E. M. Hashem, M. Mahrous Abodouh, M. S. El-Shall and S. T. Sreenivasan, *J. Am. Chem. Soc.*, 2021, **143**, 4064–4073.
37 X. Zheng, H. Wu, Y. Gao, S. Chen, Y. Xue and Y. Li, *Angew. Chem., Int. Ed.*, 2024, **63**, e202316723.
38 Q. Liu, Z. Guo, C. Wang, S. Guo, Z. Xu, C. Hu, Y. Liu, Y. Wang, J. He and W.-Y. Wong, *Adv. Sci.*, 2023, **10**, 2207545.
39 Y. Zhang, Z. Liu, C. Guo, T. Chen, C. Guo, Y. Lu and J. Wang, *Appl. Surf. Sci.*, 2022, **571**, 151284.
40 K.-Q. Lu, Y.-H. Li, F. Zhang, M.-Y. Qi, X. Chen, Z.-R. Tang, Y. M. Yamada, M. Anpo, M. Conte and Y.-J. Xu, *Nat. Commun.*, 2020, **11**, 5181.
41 Z. Li, X. Zhang, Y. Teng, H. Zhang, T. Xu and F. Teng, *ACS Appl. Mater. Interfaces*, 2024, **16**, 61921–61933.
42 T. Wang, X. Li, W. Dai, Y. Fang and H. Huang, *J. Mater. Chem. A*, 2015, **3**, 21044–21050.
43 D. Tuncel and A. N. Ökte, *J. Chem. Technol. Biotechnol.*, 2023, **98**, 2925–2942.
44 H. Haroon and K. Majid, *New J. Chem.*, 2020, **44**, 18380–18388.
45 Y. Quan, G. Wang and Z. Jin, *ACS Appl. Energy Mater.*, 2021, **4**, 8550–8562.
46 P. Nagababu, Y. T. Prabhu, A. Kularkar, M. Subbalakshmi, J. Nagarkar and S. Rayalu, *Emergent Mater.*, 2021, **4**, 503–514.
47 S. Khalil, A. Ganguly, D. Mariotti and S. Chakrabarti, *Mater. Horiz.*, 2025, **12**, 862–876.
48 G. A. Bodkhe, B. S. Hedau, M. A. Deshmukh, H. K. Patil, S. M. Shirsat, D. M. Phase, K. K. Pandey and M. D. Shirsat, *Ceram. Int.*, 2020, **8**, 803.
49 W.-T. Chen, Y. Dong, P. Yadav, R. D. Aughterson, D. Sun-Waterhouse and G. I. Waterhouse, *Appl. Catal., A*, 2020, **602**, 117703.
50 S. Yang, C. Guo, X. Huang, Y. Wang, Y. Niu, C. Liu, J. Wang and Y. Zhang, *Appl. Organomet. Chem.*, 2024, **38**, e7594.
51 J. Zhang, X. Cui, Y. Zhou, T. Kong, Y. Wang, X. Wei and Y. Xiong, *Chem. Commun.*, 2023, **59**, 2299–2302.
52 W. Cheng, Y. Wang, S. Ge, X. Ding, Z. Cui and Q. Shao, *Adv. Compos. Hybrid Mater.*, 2021, **4**, 150–161.
53 B. Jaksani, R. Chauhan, S. D. Kshirsagar, A. Rana, U. Pal and A. K. Singh, *Chem. Commun.*, 2024, **60**, 14212–14215.
54 S.-Y. Han, D.-L. Pan, H. Chen, X.-B. Bu, Y.-X. Gao, H. Gao, Y. Tian, G.-S. Li, G. Wang, S.-L. Cao, C.-Q. Wan and G.-C. Guo, *Angew. Chem., Int. Ed.*, 2018, **57**, 9864–9869.
55 T. Grewe and H. Tüysz, *ACS Appl. Mater. Interfaces*, 2015, **7**, 23153–23162.
56 H. Wang, H. Jiang, P. Huo, M. F. Edelmannova, L. Čapek and K. Kočí, *J. Environ. Chem., Eng.*, 2022, **10**, 106908.